

Nanobonding Technology Toward Electronic, Fluidic, and Photonic Systems Integration

M. M. R. Howlader, P. R. Selvaganapathy, M. Jamal Deen, *Fellow, IEEE*, and T. Suga, *Member, IEEE*

(Invited Paper)

Abstract—In this paper, a review of surface-activation-based nanobonding technology for packaging and integration is presented. In this paper, the focus will be on nanobonding technology for electronic, photonic, and fluidic devices for miniaturized biomedical- and environmental-sensing systems. We describe four different nanobonding techniques that have been developed and successfully implemented in a wide range of materials that include metals, semiconductors, flexible laminations, and ionic materials. Nanobonding technologies are particularly attractive because they offer void-free, strong, and nanoscale bonding at room temperature or at low temperature ($<200^{\circ}\text{C}$), and without the need for chemicals, adhesives, and high external pressure. Therefore, there are significant potential and opportunities for nanobonding technologies in the development of low cost, low loss, and high-speed miniaturized emerging systems based on a combination of electronic, fluidic, and photonic devices.

Index Terms—Electronic, fluidic and photonic packaging, heterogeneous integration, nanobonding, spontaneous interfacial adhesion, surface roughness and activation.

I. INTRODUCTION

THE INTEGRATION of electrical, optical, and photonic functionalities on the same substrate is a key challenge in packaging, especially for miniaturized, low-cost, and high-sensitivity biomedical- and environmental-sensing systems. For these applications, direct bonding is a particularly attractive option because it requires less space, increases the data transmission rates, offers high-performance functionality of each component, and enhances the overall system's performance. However, current bonding and packaging technologies, such as thermocompression bonding, fusion bonding, or adhesive bonding, are incompatible for many system integration applications

Manuscript received July 20, 2010; revised August 20, 2010; accepted September 12, 2010. Date of publication November 8, 2010; date of current version June 8, 2011. This work was supported by discovery grants from the Natural Science and Engineering Research Council of Canada and a major infrastructure from the Canada Foundation for Innovation under Grant 12128. The work of M. J. Deen was supported by the sponsorship of the Ministry of Education, Science, and Technology Program under Project R31-2008-000-10100-0.

M. M. R. Howlader and M. J. Deen is with the Department of Electrical and Computer Engineering, McMaster University, Hamilton, ON L8S 4K1, Canada (e-mail: mrhowlader@ece.mcmaster.ca; jamal@mcmaster.ca).

P. R. Selvaganapathy is with the Department of Mechanical Engineering, McMaster University, Hamilton, ON L8S 4L7, Canada (e-mail: selvaga@mcmaster.ca).

T. Suga is with the Department of Precision Engineering, The University of Tokyo, Tokyo 113-8656, Japan (e-mail: suga@pe.t.u-tokyo.ac.jp).

Color versions of one or more of the figures in this paper are available online at <http://ieeexplore.ieee.org>.

Digital Object Identifier 10.1109/JSTQE.2010.2080261

(e.g., biomedical systems with biological specimens or optical systems requiring high-alignment accuracies) due to the needs of high pressure [1], elevated temperatures [2], or chemical solvents [3]. An example of such an existing integration technology is 3-D integration using Cu through-silicon vias (TSVs), which requires high-bonding forces [1] and high temperatures [4].

Important challenges of current bonding techniques are the difficulty to integrate dissimilar and temperature sensitive materials with small dimensions, the inaccuracies in optical alignment, or deformation of optical components, such as polymer lenses and delicate microelectro mechanical systems (MEMS) devices [5]. Current bonding and packaging technologies do not provide the required 1) high-bond strength; 2) high-electrical conductivity; 3) hermetic sealing; 4) submicrometer alignment accuracy; and 5) optical transparency of the bonded interface between device and substrate without degrading the performance of individual components. However, the proposed nanobonding technologies meet these requirements.

Recently, in the integration and packaging field, the integration of heterogeneous technologies to create miniature, high-performance, low-cost biomedical systems, such as the wireless imaging capsule for diagnosis of the human gastrointestinal (GI) tract [6] has attracted considerable attention. For such systems, typically, we are required to integrate materials, components, and devices from photonic, optoelectronic, mechanical, and microfluidic technologies with silicon (Si) CMOS electronics. However, the integration requirements of such diverse technologies for emerging biomedical and environmental systems applications are very challenging due to incompatibilities in size and performance characteristics.

These challenges and incompatibilities can be understood from Fig. 1 that shows a 3-D plot of speed, size, and cost (plus switching energy). Here, incompatibilities are indicated when using components from emerging technologies, such as molecular, quantum, plastic, optical, and micro/nanoelectromechanical systems (M/NEMS) [7] for these emerging systems. Further, differences in the operation time for quantum, biologically inspired, and optical computing systems can be aggravated if the bonded interfaces have high resistance, high capacitance, low transparency, weak adhesion, or analyte adsorption. For example, low adhesion between interconnections and processing units may separate interconnections from a pacemaker circuit, resulting in loss of response, intermittent, or total loss of telemetry or no output from the pacemaker [8]. In addition, poor adhesion properties can have a severe affect on a system's performance when miniaturized structures with wide range of surface

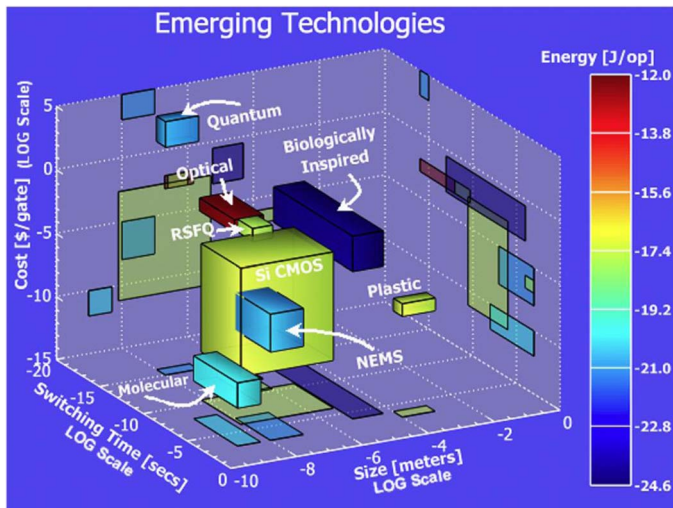


Fig. 1. 3-D plot of speed, size, cost, and switching energy components of emerging technologies, such as molecular, quantum, plastic, optical, and NEMS [7] required for the emerging systems.

morphologies and fragility associated with heat-sensitive devices are involved in the integration.

To address the challenges in direct bonding technologies resulting from high temperature (fusion and thermocompression), high pressure (thermocompression), chemical (hydrophobic and adhesive), and limited flexibility (anodic and laser assisted), surface-activation-based nanobonding technologies have been developed. These nanobonding technologies refer to the direct bonding of smooth surfaces of similar or dissimilar materials at lateral dimensions with nanometer resolution. The nanobonding processes also result in high adhesion between the mated surfaces due to the atomic forces of the activated surfaces. Therefore, surface roughness is an important parameter that controls the nanobonding. Fig. 2 shows the approaches in nanobonding technologies that are broadly classified as follows.

- 1) Nanobonding in ultrahigh vacuum (UHV) that includes (a) direct and (b) nanolayers adhesion.
- 2) Nanobonding in air that includes (c) sequential plasma activation and (d) hybrid adhesion (sequential plasma activation + electrostatic).

II. NANOBONDING METHODS AND MATERIALS

Four techniques can be used in nanobonding. In the first approach, the mating surfaces are cleaned with an argon fast atom beam (Ar-FAB), and direct adhesion occurs when they are contacted in UHV. In the second approach, the surface cleaning and nano-adhesion layer deposition are simultaneously done using an Ar ion source followed by contact in UHV. In the third approach, the surfaces are cleaned by a RF reactive-ion etching (RIE) plasma and microwave (MW) neutral radicals at low vacuum, and then, bonded in air. In all three approaches, the cleaned surfaces are called the activated surfaces. The second and third approaches have been developed for ionic materials to alleviate their surface activation induced polarization effect. In the fourth approach, the bonded wafers in the third approach are treated with an anodic bonding method (i.e., a voltage is applied on

the bonded wafers during heating at low temperature) in air. The advantages of the nanobonding over other bonding methods are

- 1) bonding dissimilar materials with high-bond strength;
- 2) no requirement of applying external pressure, adhesive, heat, or chemicals;
- 3) submicrometer alignment accuracy;
- 4) biologically compatible (i.e., nontoxic) interface;
- 5) preserves delicate components and biological specimens;
- 6) mechanical, electrical, and optical connections on the same surface.

Therefore, it is a highly promising technology that can be used to achieve novel systems combining dissimilar technologies or devices.

There are many applications of nanobonding. In Table I, we present a summary of a number of applications of the nanobonding technologies. The table includes the specifications of specimens, activation sources, surface, bonding conditions, and nanobonding approaches used in this study. For the bonding of metals, the diameter, height, and pitch are varied from 3 to 55 μm , from 0.006 to 150 μm , and from 10 to 300 μm , respectively. For bonding of semiconductors, unless otherwise mentioned, commercially available (100) wafers were used. The diameters and thicknesses of the wafers ranged from 50 to 200 mm, and from 0.275 to 0.730 mm, respectively. The vacuum pressures in the chamber required for surface activation were 1 Pa and 10^{-3} to 10^{-7} Pa, in air and UHV, respectively. The bonding pressure was varied from hand applied pressure to 0.07 to 322 MPa. With the exception of Cu/liquid crystal polymer (LCP) and Si/Ge, no other specimens were heated in pre- and postbonding, and the specimens were bonded using the fourth approach. Due to space limitations, for the detailed specifications, interested readers can consult the relevant references given in the figure captions.

III. NANOBONDING IN UHV

A. Direct Bonding at Room Temperature

1) *Smooth Surfaces of Cu Nanobumps*: An innovative ultrahigh-density interconnection was demonstrated using fine-pitch copper (Cu) bumps in [9] using the approach, as shown in Fig. 2(a). Copper wires (electrodes) with copper bumps were fabricated on wafers with a SiO_2 insulating layer. The copper bumps were planarized by a chemical-mechanical polishing (CMP) process, which resulted in Cu structures with 60–100 nm high bumps. Due to their tiny heights, the bumps in the Cu structures are regarded as bumpless. The diameter and pitch of the bumps were 3 and 10 μm , respectively. The diameters of the Cu electrodes were 3, 8, and 10 μm . The rms roughness of CMP processed Cu surface was 0.5 nm. The bumps were bonded after surface activation using a 1.5-keV Ar-FAB with current of 15 mA for 20 min. A daisy chain structure was formed after the bonding under an external pressure of 11 MPa and the interfacial contact resistance was measured.

Fig. 3(b) shows the daisy chain resistance for 3 μm sized 100 K electrodes. Included in this figure are the results of bonding for patterns with wiring problems, alignment problem,

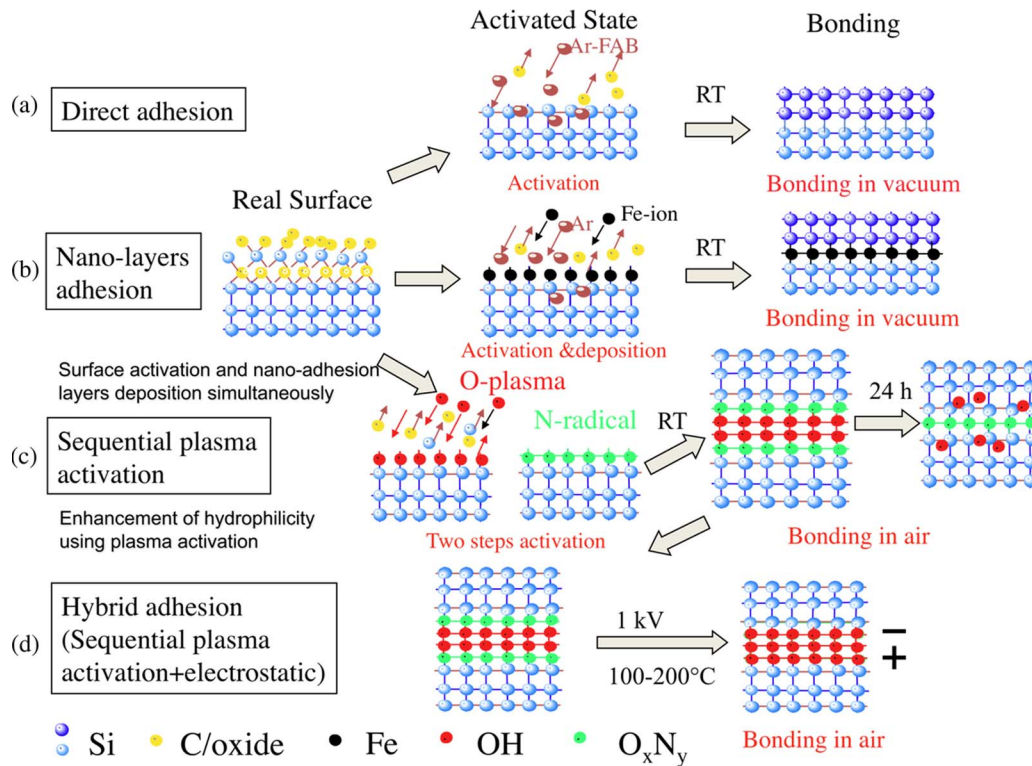


Fig. 2. Schematic diagram for surface-activation-based nanobonding technologies that provide atomic-level bonding through (a) direct adhesion, (b) nanolayers adhesion, (c) sequential plasma activation, and (d) hybrid adhesion (i.e., the enhancement of adhesion of sequentially plasma-activated surfaces through electrostatic force in anodic bonding) between the mated surfaces. Four types of surface activation have been developed based on the nature of the mated surfaces.

and good alignment. For successful bonding, the interfacial resistance between bumpless electrodes was estimated to be below $\sim 1 \text{ m}\Omega$, after subtracting the resistance of the copper wires. The contact resistance was observed to be dependent on the diameters of electrodes. The larger the diameter, the lower was the contact resistance. This was contributed mainly by the alignment error. Poor alignment resulted in failure in achieving the daisy chain interconnection of 100 K bumpless electrodes. Owing to the atomic-level bonding, the shear test showed fracture from the bottom of the copper bumps, but not from the bonded interface. From comparative reliability tests, the electrical conductance and the mechanical strength of the bonded bumps were higher than that of conventional wire bonding process [10].

2) *Rough Surfaces of Au/Cu-TSV*: Currently, 3-D system integration, such as CMOS sensors using Cu-TSVs is not only being used in production but it is also a priority area of research in academia and companies. Future applications for stacked die for memory devices with TSV will include mixed architectures like analog, logic, processor, memory, and sensors. The size and thickness of TSV need to be reduced in order to achieve miniaturized high-performance systems at low cost. For example, by 2014, the size and thickness of TSVs will be lower than 1 and 20 μm , respectively [7]. The die-to-wafer and wafer-to-wafer bonding for systems assembly and packaging using such structures with small dimensions and rough surfaces are challenging. As shown in Fig. 4, rough surfaces of gold-stud bumps (Au-SBs) have been bonded with that of Cu-TSVs at room temperature. Standard Au-SBs were flattened using an external compressive pressure about 40 MPa over each bump (external

force 0.16 N/bump) to improve the surface roughness [11]. A number of Cu-TSVs (1 20) were vertically sandwiched between chips 1 and 2 with Au-SBs. The dimensions of chip 1, TSV chip and chip 2 were 15×15 , 13×13 , and $12 \times 12 \text{ mm}^2$.

Fig. 4 also shows the top view of Au-SB and Cu-TSV, fracture images of bonded interface of Au-SB/Cu-TSV and the cross-sectional image of Au-SB/Cu-TSV. The surface roughness of the deformed area over $10 \times 10 \mu\text{m}^2$ was 9.6 nm. The surface roughness of the TSV over an area of $10 \times 10 \mu\text{m}^2$ was 6.0 nm (measured using atomic force microscope (AFM) (ICON from Veeco)). This is higher than that required for nanobonding. Therefore, an external bonding force of 20 N was used for the bonding at room temperature. The compressive pressure is about 3.5 times lower than that of used in [1].

However, for room temperature bonding [1], a mechanical-caulking technique has been implemented to bond Au-SBs with TSVs by squeezing the former into the latter by applying a compressive pressure. The cross-sectional view of the bonded interface of Au-SB and Cu-TSV shows that there is no considerable misalignment throughout the whole bonding area. The bonding strength was investigated using a tensile strength tester from Instron. After the tensile pulling test, bulk fractures in the Au-SB were observed. The fractured Au bump remained on the Cu-TSV, as shown in Fig. 4(c) (left side). The bonding of the rough surfaces of Au-SBs and Cu-TSVs is attributed to the surfaces being free of native oxides and carbon contaminations [12] with higher contact area under comparatively lower external compressive force. The electrical resistance of the interface (i.e., the two interfaces of Au-SBs and Cu-TSVs, including

TABLE I
SUMMARY OF SPECIFICATIONS OF SPECIMENS, ACTIVATION SOURCES, SURFACE, BONDING CONDITIONS, AND NANOBONDING APPROACHES USED IN THIS STUDY

Specimen	Diameter (D), height (H), pitch (P), length (L), width (W), thickness (T) [mm]	Ar-FAB (AF) and Ar-ion (AI) [keV], O ₂ RF (OR) and N ₂ MW (NM) plasma [kW], current (I) [mA], time (t) [min]	Vacuum [Pa] and bonding pressure [MPa]	Activated surface roughness [nm] over area [μm^2]	Post-bonding heating [°C], time [h], and applied voltage [kV]	Figure and approach
Cu bumps/Cu bumps	0.003 (D), 0.00006 (H), 0.01 (P)	1.5 (AF), 15 (I), 20 (t)	2×10^{-3} 11	0.5 1×1	No	3 2(a)
Cu-TSVs/Au-stud bumps	[0.055 (D), 0.150 (H), 0.3 (P)]/[0.050 (D), 0.037 (H), 0.3 (P)]	1.5 (AF), 48 (I), 5 (t)	1×10^{-7} 40	6.0/9.6 10×10	No	4 2(a)
Si/Si	50 (D), 0.275 (T)	1.5 (AF), 48 (I), 5 (t)	1×10^{-7} 0.76	0.1 1×1	No	5 2(a)
Si/GaAs, Si/InP and Si/GaP	5 (L), 5 (W), 0.45 (T)/ 10 (L), 10 (W), 0.35 (T)	1.5 (AF), 15 (I), 1.5–3 (t)	1×10^{-7} 16	0.2–0.3 1×1	No	6, 7 2(a)
GaAs/GaP	10 (L), 10 (W), 0.35 (T)/20 (L), 20 (W), 0.25 (T)	1.5 (AF), 15 (I), 3 (t)	1×10^{-7} 6	0.25 1×1	No	7 2(a)
Ce:YIG/LiNbO ₃	50 (D), 0.275 (T)/100 (D), 0.4 (T)	0.08 (AI), 3000 (I), 5 (t)	1×10^{-6} $\sim 1 \times 10^{-7}$ 0.3	– –	No	8 2(a)
Si/LiNbO ₃	200 (D), 0.73 (T)/100 (D), 0.4 (T)	0.08 (AI), 3000 (I), 1–36 (t)	1×10^{-6} $\sim 1 \times 10^{-7}$ 0.06	– –	No	9, 10 2(b)
Cu film/Liquid crystal polymer (LCP)	300 (L), 175 (W), 0.035–0.05 (T)	0.6–0.7 (AR), 30/8 (t)	3×10^{-3} 322	– –	240 1 –	11 2(b)
Si/Si	100 (D), 0.5 (T)	0.2 (OR), 0.5–1 (t) + 2 (NM), 0.5 (t)	1 Hand applied pressure	0.13–16.2 2×2	No	12, 13 2(c)
Si/Ge and SiO ₂ /Ge	50 (D), 0.275 (T)/50 (D), 0.525 (T)	0.2 (OR), 0.5 (t) + 2 (NM), 0.5 (t)	1 0.08	0.13/0.23 and 0.10/0.23 2×2	200 4 –	14 2(c)
Glass/glass	125 (D), 1 (T)	0.2 (OR), 1 (t) + 2 (NM), 1 (t)	1 Hand applied pressure	1 2×2	No	15 2(c)
Si/glass	100 (D), 0.525 (T)/100 (D), 0.5 (T)			0.18/0.46		
Ge/glass	50 (D), 0.525 (T)/100 (D), 0.5 (T)	0.05 (OR), 0.25 (t) + 2.5 (NM), 0.5 (t)	1 0.07	0.2/0.46 and –/0.46 2×2	200 0.16 1	16–18 2(d)
GaAs/glass	50 (D), 0.35 (T)/100 (D), 0.5 (T)					

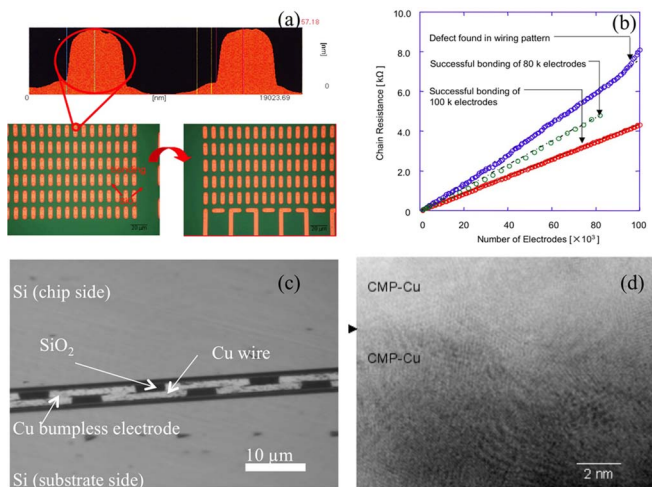


Fig. 3. (a) AFM image of Cu nanobumps showing the height, (b) daisy chain resistance for 3 μm size 100 K electrodes, (c) SEM image of the cross section of Cu/Cu bonded interface, and (d) HRTEM image of the bonded interface. Arrows indicate the bonded interface [9].

the height of one Cu-TSV) was as low as 0.5 Ω [11], [12]. This interfacial resistance (0.5 Ω) is considerably higher than that in the smooth surfaces of Cu nanobumps (~ 1 m Ω). The higher resistance is caused by the higher surface roughness of Au-SB and Cu-TSV and the resistance of Cu-TSV.

Recently [13], it has been reported that the bonding temperature of Cu nanorods and nanowires (NWs) can be reduced due to their small area. In fact, atomic-level bonding was demonstrated using the smooth surface of Cu nanobumps and rough surfaces of Au and Cu-TSV at room temperature and low-bonding pressure. Furthermore, submicrometer alignment accuracy with electrical resistivity of Cu/Cu interface that is equivalent to bulk materials of Cu was observed. This implies that the existing interconnections through direct bonding of Cu–Cu will be replaced by NWs and nanostructures-based emerging systems. Therefore, the nanobonding approach can be used not only for the high-density interconnection in systems' integration but also for high-speed systems with NWs and nanostructures. Such nanostructures can be quickly built in a controlled manner using nanoimprint technology [14].

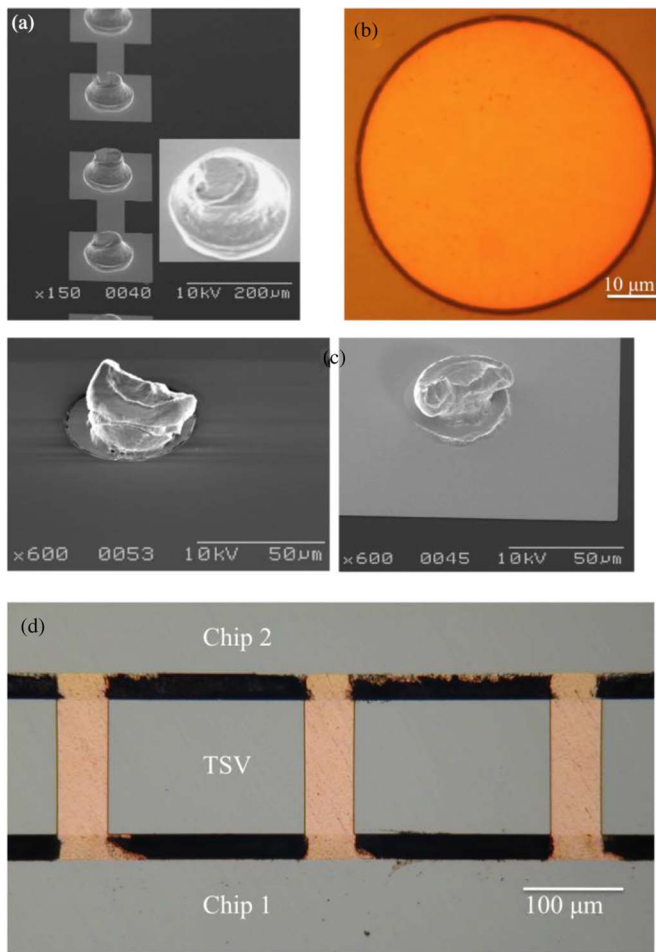


Fig. 4. Top views of (a) Au-SB and (b) Cu-TSVs (c) fracture images (Au remained on Cu-TSV at left side and broken Au bump at right side) of Au-SB/Cu-TSV bonded interface after tensile pulling test, and (d) the cross-sectional image of Au-SB/Cu-TSV [11].

3) *Si Wafers*: While surface characteristics, such as roughness and type of bonds and their lengths, of semiconductors are different from metals, identical surface activation using Ar-FAB as well as bonding in UHV have been demonstrated for various semiconductors [15]–[21]. Fig. 5 shows the AFM images of a Si surface before and after activation, and the Si/Si interface bonded using the first approach described earlier in Section II. The wafers were p-type and the resistivity was 1–20 Ω ·cm. The activation sources were placed at 45° with respect to the center of the specimens and the surfaces were homogeneously activated throughout the 2 in diameter wafer. The clean and smooth surfaces, after activation, control the quality of the bonded interfaces, which is critical for the successful fabrication of electronic devices. While the surface roughness before activation was 0.17 nm, it became 0.11 nm after activation for 300 s using a 1.5 keV Ar-FAB.

Fig. 5(c) shows the IR image of Si/Si interface bonded at room temperature after activation for 300 s using the FAB. Spontaneous bonding was observed in the UHV after the surface activation [15]. Using infrared transmission images, the image shows no voids (unbonded area) across the interface. Also, no interfacial voids have been observed at the Si/Si interface for

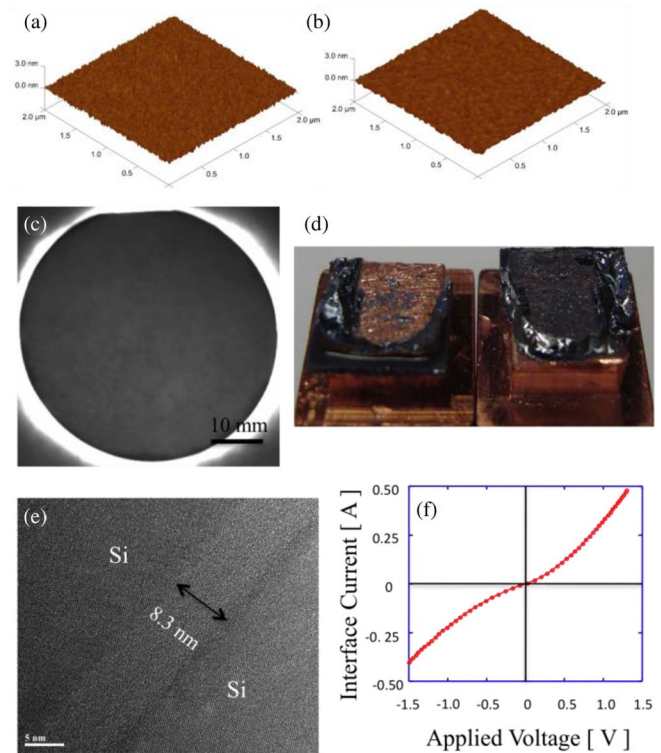


Fig. 5. Images of Si surface (a) before and (b) after surface activation using AFM. Images of (c) infrared transmission, (d) fractures, and (e) HRTEM with (f) I - V characteristics of the p-Si/p-Si bonded junction. The surfaces were activated by a 1.5 keV Ar-FAB with 48 mA for 300 s and bonded in UHV at room temperature [16].

postannealing in air up to 600 °C [16]. The fracture image of Si/Si bonded interface after tensile pulling test showed bulk fractures remained on the Cu-jigs on both sides [see Fig. 5(d)]. Fig. 5(e) shows the high-resolution transmission electron microscope (HRTEM) image of Si/Si bonded interface for the 300 s activation time. No microvoids were found at the interface. However, a 8.3-nm-thick amorphous layer was present at the bonded interface. This amorphous layer was caused by the Ar ions inducing defects on the Si surfaces during the activation and forming a damaged layer on the Si surfaces. Although the amorphous layer was at the interface, bonding strengths as high as 18 MPa were achieved at room temperature. This bonding strength was higher than that using sequentially plasma-activated bonding (SPAB) or hydrophilic bonding. The bonding strength showed no changes after postannealing up to 600 °C, which is suitable for high-temperature applications. The measured I - V characteristic of bonded p-Si/p-Si junction was shown in Fig. 5(f). Typical I - V curve of p-p junction was observed.

4) *Si/III-V Semiconductors*: In the first approach described in Section II, heterogeneous semiconductor wafer bonding such as Si/InP, Si/GaAs, Si/GaP, and GaP/GaAs for photonic applications, was reported after surface activation by Ar-FAB in a UHV chamber [17]. These surfaces before and after activation were comprehensively investigated by X-ray photoelectron spectroscopy (XPS) (from Perkin-Elmer) using a monochromatic Mg $K\alpha$ X-ray radiation source at 15 kV and 400 kW. Fig. 6(a) and (b) show typical XPS spectra of Si and GaAs

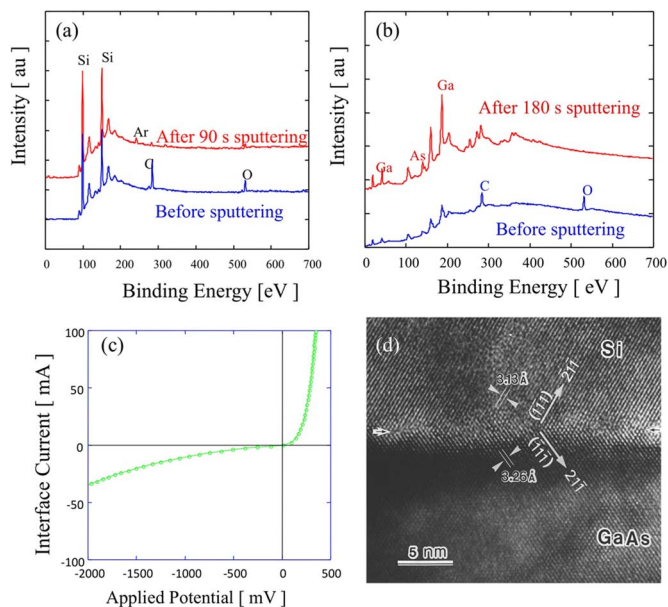


Fig. 6. XPS spectra for (a) Si and (b) GaAs surfaces before and after activation. (c) I - V characteristics of the p-Si/n-GaAs bonded junction and (d) HRTEM of Si/GaAs interface [17], [18].

surfaces before and after surface activation. While XPS peaks for carbon and oxygen were observed on the surfaces before activation, these peaks disappeared after activation [17]–[19]. This indicates cleaned and activated surfaces. Identical XPS spectra were observed for InP and GaP. The surface roughness before activation was in the range of 0.2 to 0.25 nm [19], [21]. Therefore, there was no significant increase in the surface roughness after activation, and it was much below the surface roughness requirement for the nanobonding method (i.e., <1 nm rms). Therefore, similar to the Si surface, the clean, smooth, and activated InP, GaAs, and GaP surfaces were appropriate for spontaneous bonding at room temperature.

Fig. 6(c) shows the I - V behavior of p-Si/n-GaAs bonded wafers using the nanobonding technology in UHV. The electrodes for Si and GaAs were made by Au and Au/Ge with 3 mm diameter before bonding for the ohmic contacts. The measured I - V characteristic of p-Si/n-GaAs shows typical I - V curves of a p-n junction. The p-n junction can be analyzed by the thermionic emission theory in order to evaluate the ideality factor of the junction. However, the values of ideality factor for bonded p-Si/n-GaAs wafers were from 3 to 3.5 [17]. The high-ideality factor of bonded wafers can be attributed to the presence of an interfacial layer between Si and GaAs. This interfacial layer can be affected by the activation energy and time. The influence of the Ar-FAB energy and activation time on the current density of the p-n junction was observed, as well as the influence of the exposure time in the UHV atmosphere.

Fig. 6(d) shows the HRTEM of Si/GaAs bonded interface. Atomic-scale bonding between Si and GaAs was observed without any cracks and voids at the interface [18]. This is attributed to the spontaneous covalent bonding at room temperature due to the direct adhesion between nanometer-scale smooth and clean surfaces. In contrast to the Si/GaAs p-n junction, ideal p-n junc-

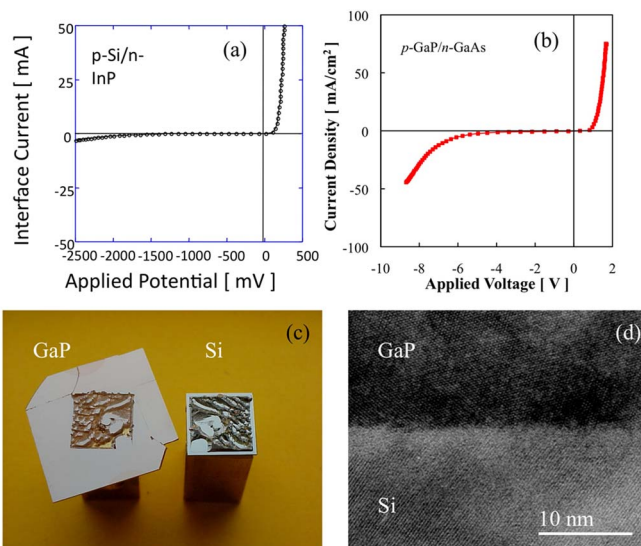


Fig. 7. I - V characteristics of (a) p-Si/n-InP and (b) p-GaAs/n-GaP interfaces. (c) Fracture images of Si/GaP and (d) HRTEM of Si/GaP interface [19]–[21].

tion behavior of bonded p-Si/n-InP [18] and p-GaP/n-GaAs [21] was confirmed by I - V measurements, as shown in Fig. 7(a) and (b). Also, the bonded interfaces exhibited high strength, which can be observed through the fracture images of Si/GaP after the tensile pulling test, as shown in Fig. 7(c). The HRTEM image shows atomic-scale bonding (with poor visibility), similar to the Si/GaAs interface [see Fig. 7(d)].

To summarize the nanobonding of semiconductors, chips from wafers of different III-V semiconductors were bonded with Si by the nanobonding approach, as shown in Fig. 2(a), after surface activation that removes native oxides, contaminations, and makes the surface smooth. The good quality of the Si/Si bonded interface after surface activation by Ar-FAB in UHV chamber was demonstrated. Almost perfect bonded interfaces at the atomic level were achieved by the proper choice of surface activation parameters. The quality of the interface was confirmed by electrical measurements of the p-n junction at this interface [see Fig. 6(c)] and by HRTEM [see Fig. 6(d)]. The bonded interfaces also exhibited high strength, allowing CMP for thinning of a bonded chip to few micrometer, as required for photonic applications.

5) $CeY_2Fe_5O_{12}(Ce:YIG)/LiNbO_3$: In optical communications systems, optical isolators are indispensable to protect optically active devices from unwanted reflected light. The integration of optically active devices with a waveguide optical isolator is in high demanded for low-cost and high-performance optical sources [22]–[25]. One optical isolator is the semileaky waveguide optical isolator. It consists of a magneto-optical guiding layer and an optically anisotropic cladding layer, as shown in Fig. 8(a). This isolator consists of a substrate: $(GdCa)_3(GaMgZr)_5O_{12}$ (NOG), guiding layer: $(CeY)_3Fe_5O_{12}$ (Ce:YIG), and an upper cladding layer: lithium niobium oxide ($LiNbO_3$). The advantages of this isolator are its compact structure, easy control of magnetization, wide operating wavelength range, and large fabrication tolerance [23]. However, the

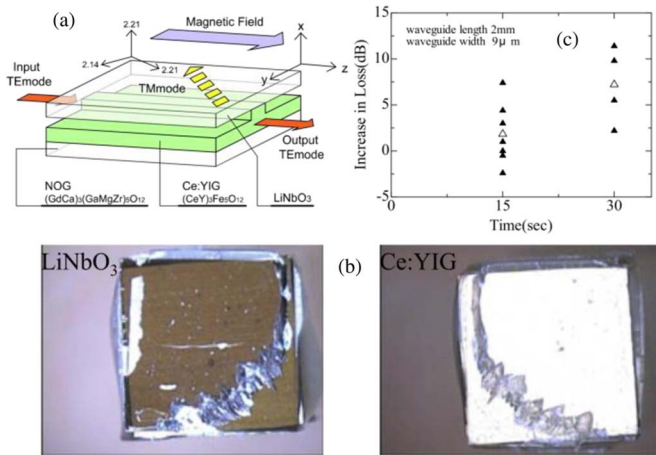


Fig. 8. (a) Schematic of semileaky-type optical isolator, (b) fracture images of LiNbO₃ (left)/Ce:YIG (right), and (c) low-energy Ar ion beam activation time versus loss of Ce:YIG waveguide [24].

difficulty is to achieve the tight and homogeneous optical contact between the magneto-optic and the optically anisotropic crystal using conventional bonding technologies. Then, the nanobonding technology in the UHV has been investigated for bonding dissimilar crystals directly. For example, Ce:YIG (2 in) and LiNbO₃ (4 in) were successfully bonded after surface activation by Ar-FAB. The bonded wafers were diced into $1 \times 1 \text{ cm}^2$ for the tensile pulling test [24].

Fig. 8(b) shows the fracture image of Ce:YIG/LiNbO₃. The average value of the bonding strength was 11.9 MPa. From the results of tensile pulling test, strong bonding strength was realized by using surface activation bonding at room temperature. Optimization of the optical performance of the isolators and the surface activation parameters must be taken into account. In order to compare the optical characteristics of Ce:YIG waveguide before and after the ion irradiation, the waveguide loss was measured by changing the irradiation time with a fixed Ar-FAB energy. The wavelength of the laser used was 1550 nm and it operated in the TM mode. The Ce:YIG waveguide was 1190 nm thick, 9 μm wide, and 2 mm long. It turns out that the loss of the waveguide increases after long irradiation times, as shown in Fig. 8(c). However, the increase in loss could be reduced by appropriate choice of the beam irradiation conditions. An isolation ratio of 20.2 dB at a wavelength of 1550 nm in Ce:YIG/LiNbO₃ isolator has been reported [23]. Also, LiNbO₃ was successfully bonded on Ce:YIG after surface activation in a plasma generated in the gas mixture of Ar and O₂ in UHV at room temperature. In addition, Ce:YIG was directly bonded onto a Si rib waveguide based on O₂ plasma activation in UHV [25].

B. Indirect Bonding Through Nano-adhesion Layers

1) *Ionic Material (LiNbO₃) With Si at Room Temperature:* New physics-based strategy for bonding of Si to ionic materials (glasses) was developed that were verified experimentally with wafers of Si, SiO₂, silica glass, LiNbO₃, and quartz in UHV [26], [27]. While the single crystalline ionic wafers, such as LiNbO₃ and LiTaO₃ are materials of interest for the fabri-

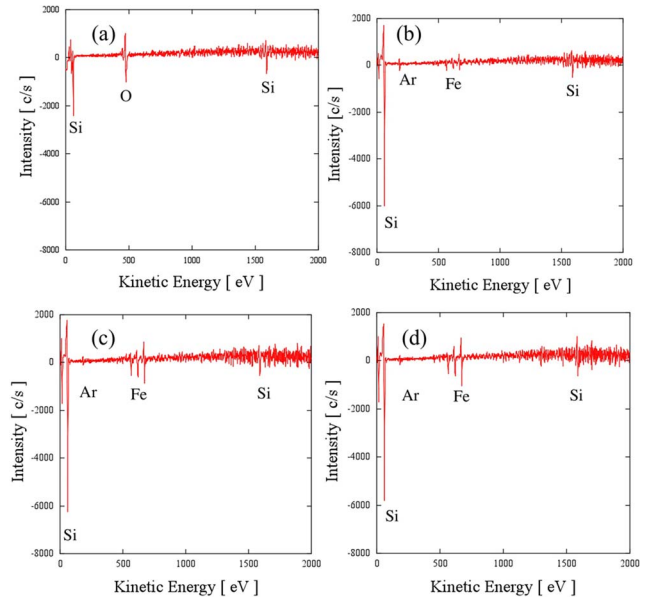


Fig. 9. (a) AES of silicon surfaces (a) before and after surface activation for (b) 1, (c) 6, and (d) 36 min using modified low-energy Ar ion source [26], [27].

cation of optoelectronic modulators, piezoelectric components, and MW tunable devices, these materials inhomogeneously polarize after surface activation. This results in repulsive force between the wafers. In order to depolarize, the surface of ionic crystals was activated for a prolonged time, while depositing ultrathin Fe layers using a modified hollow cathode-ion source. The deposition of ultrathin Fe layers was detected on Si wafer by using Auger electron spectroscopy (AES). Si was used as probe to avoid charging problems with the energetic beam on LiNbO₃.

Fig. 9 shows the AES of Si surfaces before and after sputter cleaning at 1, 6, and 36 min with the modified-ion source. The native oxides and carbon present on the surface before activation disappeared after activation for 1 min. After surface activation for 6 min, Fe counts remained constant with the increase of activation time up to 36 min. The Fe adhesion layers not only increase the bonding strength at the interface (8 to 37.5 MPa) but also maintain the optical transparency of the bonded wafers, which is very important for applications to image sensors and optical waveguides [26]. From the optical image of the Si/LiNbO₃ bonded interface [see Fig. 10(a)], one can realize that the entire area of LiNbO₃ is bonded without voids. Bulk fracture was obtained in Si after tensile pulling test of the chip from the bonded wafers [see Fig. 10(b)]. This void-free bonded interface can improve the performance of systems to be built by producing electrically and optically useful interfaces [27]. Fig. 10(c) and (d) shows the HRTEM image of Si/LiNbO₃ bonded at room temperature with electron energy loss spectroscopy (EELS) spectra. The HRTEM image shows a low-energy ion induced 5-nm-thick amorphous layer across the interface. A dark contrast region was found across the interface and the main composition of this layer was detected to be Fe by EELS analysis at the interface [26], [27].

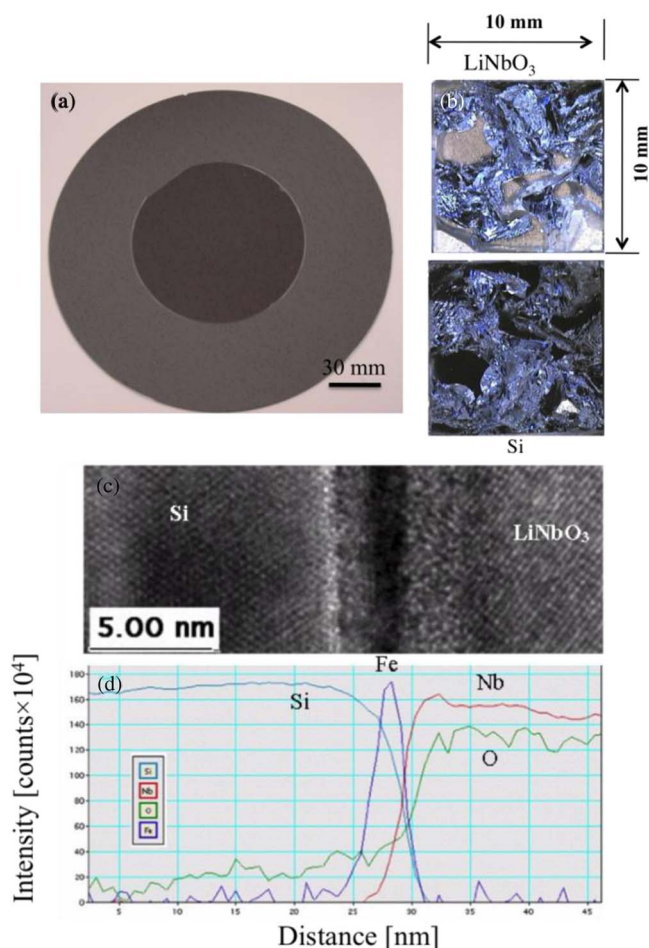


Fig. 10. Images through (a) optical, (b) fracture, and (c) HRTEM observations with (d) EELS spectra of Si/LiNbO₃ bonded at room temperature using a modified low-energy Ar ion source [26].

2) Flexible Lamination of Cu/LCP at Low Temperature:

Besides rigid materials, flexible lamination offers many advantages for lightweight, miniaturized microelectronics [28], MEMS [28]–[30], and “intelligent” biomedical microsystems [28], [31]. In case of implantable biomedical microsystems, low-water uptake and biocompatibility are crucial to avoid toxic reaction [31]. For such applications, LCP is an excellent choice because of its higher heat resistance, lower hygroscopicity, lower coefficient of hygroscopic expansion, lower coefficient of thermal expansion, and better dielectric properties compared to polyimides [32]–[34]. However, the LCP has weak adhesion with Cu. Therefore, a variety of technological approaches has been employed to enhance polyimide/metal adhesion using laser treatment [35], plasma cleaning and modification [36], [37], and metal deposition and metallization with [38]–[40] and without [38]–[40] plasma cleaning on the basis of morphological, chemical, and physical nature of polyimide and metal. Note, however, that the conventional heat lamination process for LCP with Cu degrades the LCP’s properties.

In contrast to the bonding of ionic wafers using nanoadhesion layers on the activated surfaces in UHV at room temperature [26], [27], activated polymer surfaces with nanoadhesion layers

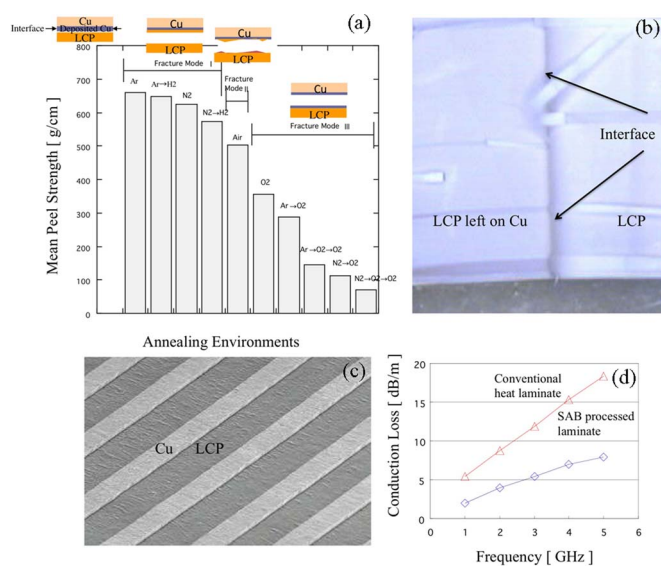


Fig. 11. (a) Peel strength of Cu/LCP as a function of annealing in different gases at 240 °C, (b) peeled surfaces of Cu and LCP, (c) SEM image of Cu on LCP after patterning and etching, and (d) conduction loss versus frequency of nanobonded Cu/LCP interface compared with conventional heat laminate [32], [34].

do not bond without heating [32]–[34]. This is due to the low adhesion resulting from the high-surface roughness of polymer surfaces after activation (and even before activation), and the deposition of nanoadhesion layers. In this approach, the Cu and LCP surfaces were sputter cleaned with Ar-RF plasma etching in a low vacuum of 10^{-3} torr to remove the inactive layers of native oxide and contaminants on the surfaces. Then, Cu was deposited on the LCP, and the two were bonded directly at room temperature [34]. Subsequently, the Cu/LCP specimens were heated in an Ar gas below the glass transition temperature of LCP. This process resulted in higher interface adhesion than that in the conventional heat-laminated process.

A comprehensive investigation of the adhesion improvement and mechanism, interface quality in terms of mechanical and electrical integrity, and fine-pitch patterning was reported in [32]–[34]. Fig. 11 shows (a) the peel strength of Cu/LCP heating in N₂, Ar, air, and O₂ gases; (b) the optical image of partially peeled Cu and LCP surfaces with the interface; (c) the SEM image of the etching patterns of Cu on LCP; and (d) the frequency-dependent conduction loss of LCP/Cu interface compared with that of conventional heat laminate. The peel strength of specimens heated in Ar and N₂ was found to be much higher than that of specimens heated in air and O₂. The peel strength in an O₂ gas medium was the lowest. The sequential heating in O₂ gas of the specimens already heated in Ar and N₂ gases reduced their peel strength. The optical image after the peeling test showed bulk fracture of LCP for the specimens annealed in an Ar environment [32], indicating higher interfacial adhesion strength than that of bulk LCP material. A plausible adhesion mechanism of Cu/LCP is the bonding of Cu adhesion sites (cleaned) to plasma-induced dangling sites of LCP surface (Cu deposited), and thermal reconstruction of Cu deposited layers when heating in Ar and N₂ gases. This is in contrast to

mechanical interlocking across the interface utilized for adhesion improvement in the conventional lamination of polymer to metal.

We now discuss laminates of Cu and LCP. The laminated Cu/LCP was patterned with the line and space for the etching patterns being $50\ \mu\text{m}$. The pattern width for Cu and LCP was 7 and $50\ \mu\text{m}$, respectively [34]. The interfaces for fine-pitch surface-activated bonding (SAB) laminates were strong enough to be flexed and are suitable for high-density flexible biomedical systems. The measured conduction loss in both the SAB and conventional laminates increases with frequency. A three-fold lower loss for the SAB laminate was observed compared with the conventional heat laminate. The rms value of the roughness for the conventional heat-laminated surface was $970\ \text{nm}$, whereas for the SAB-laminated surface, it was only $64\ \text{nm}$. The bonded interface of the laminate prepared by the SAB method is about 15 times smoother than that of the heat-laminated method. During high-speed signal transmission, since the electrical current flows only through the parts of conductors within $1\ \mu\text{m}$ of the surface due to the skin effect, then micrometer-sized roughness of the interface leads to functional failure of the electrical circuit. The mechanical and electrical integrity of flexible lamination are vital for its improved performance, especially for microcoils wrapped around small catheter tip, or for small polymer bumps [28], [41]. This method provides strong bonding without the need for adhesives, and it also produces a smooth interface that allows for fine-pitch laminates suitable for low-loss, high-frequency, or biomedical applications [42], [43].

IV. DIRECT BONDING IN AIR

A. Semiconductors at Room Temperature

For low-cost integrated system applications [44]–[49], direct bonding of wafers in atmospheric air is indispensable. This is the third approach of nanobonding technology, which is known as SPAB [50]. In this approach, as mentioned in Section I, the physical sputtering capability, i.e., removal of native oxides and contaminations, of the RIE plasma was combined with the reactivity of MW neutral radicals that allowed for bonding at room temperature without pre- and postbonding heating. While the SPAB depends significantly on the type of gases to be used for the RIE and radicals, the best combination to induce spontaneous adhesion between semiconductor wafers was found to be O_2 and N_2 gas for RIE plasma and for MW neutral radicals activation, respectively. This combination provides highly hydrophilic and smooth surfaces, as shown in Fig. 12. In Fig. 12 the AFM images of Si surface are also shown (a) before plasma activation, and after activation with (b) O_2 RIE, (c) N_2 RIE and (d) Ar RIE plasma, and (e) MW O_2 , and (f) MW N_2 radicals activation. These results indicate that O_2 RIE plasma offers the lowest surface roughness of Si among O_2 , N_2 , and Ar RIE plasma activation. An anomalous Si surface morphology was observed after Ar plasma activation, as shown in Fig. 12(d). Further research is required to fully understand these results. However, the MW N_2 radicals, resulting in a much smoother surface than MW O_2 radicals. Based on the contact angle and surface roughness results, in order to achieve lowest contact an-

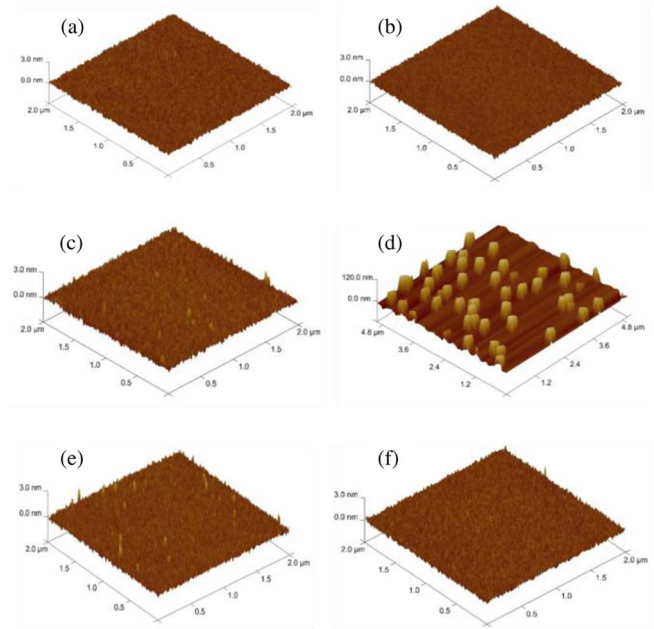


Fig. 12. AFM images of Si wafer surface (a) before activation and after activation with (b) O_2 RIE, (c) N_2 RIE, (d) Ar RIE plasma, (e) MW O_2 , and (f) MW N_2 radicals [51].

gle (highest hydrophilicity) and lowest surface roughness, O_2 gas was chosen for RIE plasma activation and N_2 gas was chosen for MW radicals' activation [51].

1) *Bonding of Si/Si*: In SPAB, the bonding strength of Si wafers was as high as $15\ \text{MPa}$, which was achieved after leaving the bonded wafers for 24 h in ambient [50], [52]. To understand the reliability of the Si/Si interface, the bonding strength was measured after annealing up to $600\ ^\circ\text{C}$ and the results compared with that before annealing. Fig. 13 shows the bonding strength versus annealing temperature in SPAB and in hydrophilic bonding for comparison. At room temperature, the bonding strength in SPAB is about 30 times higher than that in hydrophilic bonding. Although the bonding strength in SPAB decreased after annealing, it was much higher than that in hydrophilic bonding. The higher bonding strength in SPAB is due to the highly hydrophilic and reactive surfaces of Si after sequential plasma activation. Our recent study [53] confirmed the presence of nanopores on the sequentially plasma-activated surfaces. These nanopores allow for easy removal of water from the interface to the Si bulk, thereby resulting in strong covalent bonding. The decrease in bonding strength in SPAB over $300\ ^\circ\text{C}$ is attributed to the generation of thermal-induced voids at the interface.

Fig. 13(b) and (c) shows the HRTEM images of Si/Si bonded interface before annealing and after annealing at $600\ ^\circ\text{C}$ [54]. Nanoscale bonding was achieved with an amorphous layer of thickness $4.8\ \text{nm}$. No interfacial voids and defects were observed in the HRTEM images. After annealing at $600\ ^\circ\text{C}$, an abrupt change in amorphous layer thickness was observed. This is attributed to the oxidation of Si due to interfacial water. The oxidation of Si resulted in SiO_2 and H_2 at the interface. The

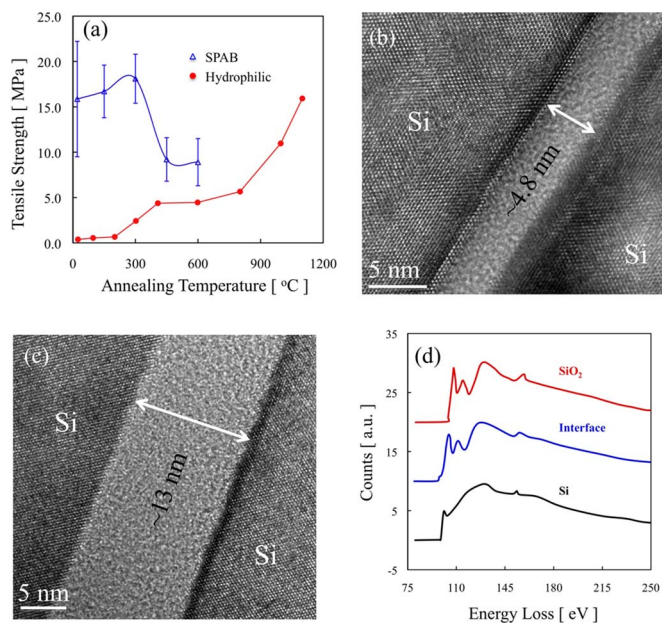


Fig. 13. (a) Bonding strength as a function of annealing temperature for SPAB and hydrophilic bonding. HRTEM images of Si/Si bonded interface (b) before annealing, and (c) after annealing at 600 °C with (d) compositional distribution at the interface of the annealed specimen, standard Si and SiO₂ [53], [54].

presence of SiO₂ was confirmed by EELS [see Fig. 13(d)], where the EELS spectra of the interface were similar to the standard EELS spectra of SiO₂. The evolution of H₂ at the interface resulted in thermal voids, and hence, is responsible for the decrease in bonding strength, as observed in Fig. 13(a).

2) *Bonding of Si/Ge and SiO₂/Ge*: Since germanium (Ge) has large absorption coefficient at the near infrared frequency range, and a high-carrier mobility, integration of Ge with Si and SiO₂ at low temperature allows for the creation of high-performance photodetectors, solar cells, and Ge-on-insulator (SiO₂) (GeOI) structures required for optoelectronic or photonic systems applications, for example, [55]–[58]. The Si/Ge and SiO₂/Ge wafers were bonded using SPAB at room temperature. However, the bonding strength of Si/Ge and SiO₂/Ge was low, and they debonded during dicing [51]. To increase the bonding strength, the bonded wafers were heated at 200 °C, and subsequently, annealed at 150 °C.

Fig. 14 shows the bonding strength of the sequentially plasma-activated Si/Ge and SiO₂/Ge wafers after annealing at 200 °C, as well as 200 °C followed by 150 °C in air for 4 h at each step. At 200 °C, while the bonding strength of Si/Ge was about 1 MPa, it was about 5 MPa for SiO₂/Ge. This difference in the bonding strength is due to the unique reactivity of Ge and its discrepant interactions with Si and SiO₂. Therefore, in terms of the reactivity, the higher reactivity difference of SiO₂/Ge than that of Si/Ge was responsible for higher bonding strength of SiO₂/Ge wafers. Further annealing at 150 °C, the bonding strength of Si/Ge was increased, but decreased in the case of SiO₂/Ge bonding. The bonding strength was relatively low compared to that of Si/Si in the SPAB at room temperature (compare Figs 13 and 14). The relatively low-bonding strength in the Si/Ge and SiO₂/Ge can

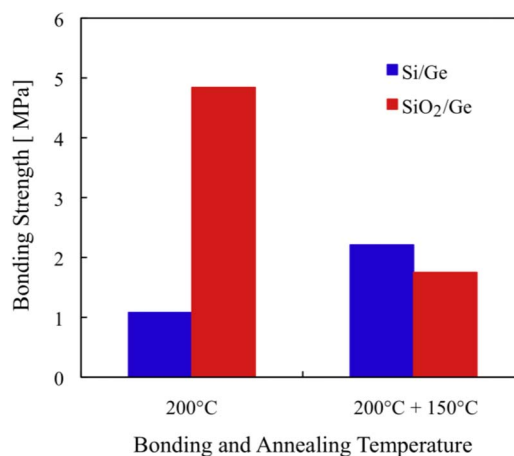


Fig. 14. Bonding strength of the sequentially bonded Si/Ge and SiO₂/Ge wafers. After contacting at room temperature, the bonded wafers were annealed in air for 4 h at each step [51].

be due to the high reactivity of Ge wafer after surface activation. It is known that Si and Ge surfaces have native oxides and the bond length of Ge–O (oxygen) is higher than that of Si–O [59]. Therefore, the O₂ RIE plasma breaks Ge–O bonds and MW N₂ radicals generate Ge oxynitride relatively easier than Si–O, thereby resulting in a large number of free dangling sites. These sites occupy higher number of OH[−] molecules on the activated Ge surface when exposed to the clean room ambient, which results in weak bonding at room temperature.

In order to improve the bonding strength, it was essential to remove the large number of OH[−] molecules across the interface. The reactions between Si/Ge and SiO₂/Ge produce water across the interface after heating at 200 °C, which needs to be diffused out of the interface. The bonding strength of SiO₂/Ge was higher compared to the Si/Ge, which was due to the absorption of water by the SiO₂ layer through the annealing process at 200 °C. Further annealing at 150 °C desorbed the water from SiO₂ and initiated a reaction at the interface of SiO₂/Ge, causing a brittle interfacial layer and reduced bonding strength of SiO₂/Ge. In contrast, after the annealing of Si/Ge in identical conditions, the remaining interfacial water was diffused through the plasma-induced oxide and reacted with the bulk of Si and Ge to form respective oxides [51]. Hence, heating at 200 °C as well as 200 °C followed by 150 °C was not sufficient to achieve covalent bonding between Si/Ge. Further research is underway at higher temperatures to achieve higher bonding strength of Si/Ge.

3) *Bonding of Glass/Glass*: In contrast to Si/Ge bonding, glass/glass wafers had strong adhesion at room temperature, which was demonstrated for glass-based microfluidic devices [60], [61]. Fig. 15 also shows the optical images for glass/glass bonded wafers and a microfluidic chip with OH[−] dependence of bonding strength. The wafers were activated using O₂ RF plasma at 30 Pa and N₂ MW radical plasma at 30 Pa for 120 s. A void-free interface with some particles inclusion was observed. The particles can be eliminated using a better clean room than the class 10 000 clean room that was used. The bonding strength was comparable to the bulk materials. This was explained

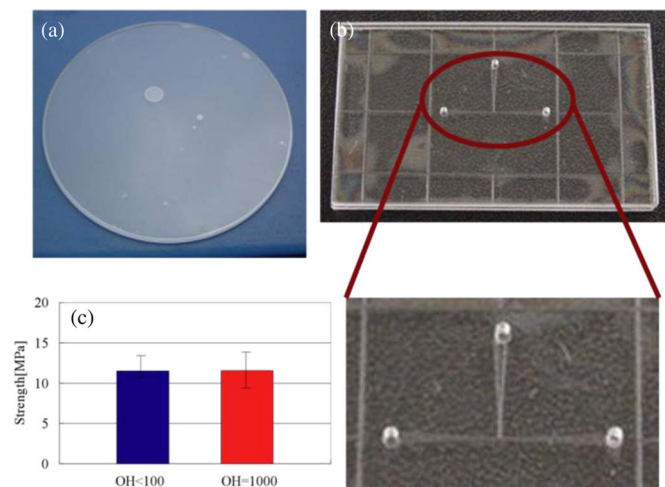


Fig. 15. Optical images of (a) glass/glass bonded wafers, (b) microfluidic chip after bonding, and (c) bonding strength of glass/glass wafers as a function of contents of hydroxyl molecules in the glass wafer [60], [61].

in terms of the reaction between sequentially plasma-induced metastable surfaces through OH^- sites on both surfaces, which resulted in water formation across the interface. The sequentially treated porous surfaces allow water to diffuse into the bulk materials and the oxynitride sites on both surfaces react and produce stabilized silicon oxynitride.

In order to clarify the role of OH^- contents in the glass wafers on the bonding strength, the bonding strength of glass wafers with $\text{OH}^- < 100$ and $\text{OH}^- = 1000$ ppm molecules in the SPAB was measured. The amplitude of the bonding strength for $\text{OH}^- < 100$ and $\text{OH}^- = 1000$ ppm wafers was 11.1 and 12.3 MPa, respectively [see Fig. 15(c)]. This result indicates that the OH^- contents had no significant effect in the glass/glass bonding strength. This is in contrast to the OH^- molecules that are induced in the sequential plasma activation and are involved in the chemical reaction between the OH^- molecules on the mating surfaces to initiate the bonding. It has also been reported that the glass/glass wafers bonding in vacuum after cleaning with RIE O_2 RF plasma and N_2 radicals MW plasma was failed. This is because, on the activated surfaces, the OH^- molecules required to initiate bonding, was not sufficient in UHV.

For the fabrication of the microfluidic chip shown in Fig. 15(b), two chip-sized glass wafers were used. One glass wafer had three 500 μm sized holes that were prepared using a mechanically mounted wheels drilling process. For the other glass chip, T-shaped microfluidic channels were fabricated using the wet chemical (HF) etching process. The depth and width of the microchannels was 60 and 120 μm , respectively. The drilled wafer was polished by mechanical and chemical polishing to smoothen the surfaces, then activated with sequential plasma activation, and finally, bonded together after manual alignment at room temperature. The bonding strength was equivalent to the bulk materials. Also, smooth surface roughness as well as UV light transparency was maintained [27], [61], [62]. The results from this study indicate that the performance of glass/glass microfluidics device makes it suitable for applications, such

as laser-induced fluorescence [62] and UV absorbance detections [63].

Although the SPAB has been implemented in the direct bonding of a significant numbers of semiconductors, metal-metal bonding has not yet been investigated using this method. In fact, the important role of gases used in the RIE and MW plasma on the surface activation was observed, as already described in Section IV. The Ar RIE plasma activation in a low vacuum (identical to sequential activation) has been utilized to directly bond Au-Au, Au-Al, and Au-Cu in air at room temperature [10]. The CMP-Cu surfaces with average surface roughness of 1–2 nm were activated using Ar-FAB in a relatively high vacuum and bonded in O_2 gas with controlled humidity under a load of 490 N at 150 $^\circ\text{C}$ [64]. The exposed pressure of the O_2 gas was 8.0×10^4 Pa and the heating time was varied from 300 to 3600 s. In O_2 exposure, a 7-nm-thick surface of Cu_2O was converted into a 10-nm-thick CuO interface because of the oxidation of Cu_2O during heating. High-bonding strength equivalent to bulk breakage of Cu film was reported [64]. The copper oxide layers increase the interfacial resistance, which is relatively high compared to that of the Ar-RIE plasma-bonded interfaces. Further research in the metal-metal bonding using SPAB would clarify its applicability to achieve electrically and mechanically functional interfaces.

B. Bonding of Ionic Materials at Low Temperature

Due to the relatively high-surface roughness of glass compared to Si, the glass/glass wafers had relatively lower adhesion than that of Si/Si wafers. Therefore, in order to increase the bonding strength for glass wafers by enhancing their surface adhesion properties, a novel bonding technique was developed. This technique is called hybrid plasma bonding (HPB) [65]. As previously mentioned, in HPB, the wafer surfaces were first activated using O_2 RIE plasma followed by MW N_2 radicals. Then, the wafers were bonded in a clean room ambient by hand-applied pressure. Finally, the bonded Si/glass pair undergoes anodic treatment using 1 kV bias at 100–200 $^\circ\text{C}$ for 10 min.

1) *Bonding of Si/Glass*: In order to clarify the role of sequential plasma activation [61] and anodic bonding [66] (i.e., temperature and voltage) in HPB, the Si and glass wafers bonded using HPB were compared with those using only anodic bonding. Although interfacial voids were observed in anodic bonding (100, 150, and 200 $^\circ\text{C}$), a void-free interface was achieved in HPB at 200 $^\circ\text{C}$. Fig. 16 shows the optical images of anodic bonded Si/glass [see Fig. 16(a)] and HPB Si/glass [see Fig. 16(b)] wafers at 200 $^\circ\text{C}$ [65]. The void-free interface was further confirmed by HRTEM observation. Fig. 16(c) shows the HRTEM images of Si/glass interface in HPB at 200 $^\circ\text{C}$. No interfacial voids or defects were observed in the HRTEM images. A ~ 353 -nm depletion layer was observed in glass due to the transportation of alkaline cations (Na^+) and anions (O^-) across the interface.

The bonding strength in HPB was compared with that in anodic bonding and the results are shown in Fig. 16(d). In the anodic bonding, while the bonding strength was significantly

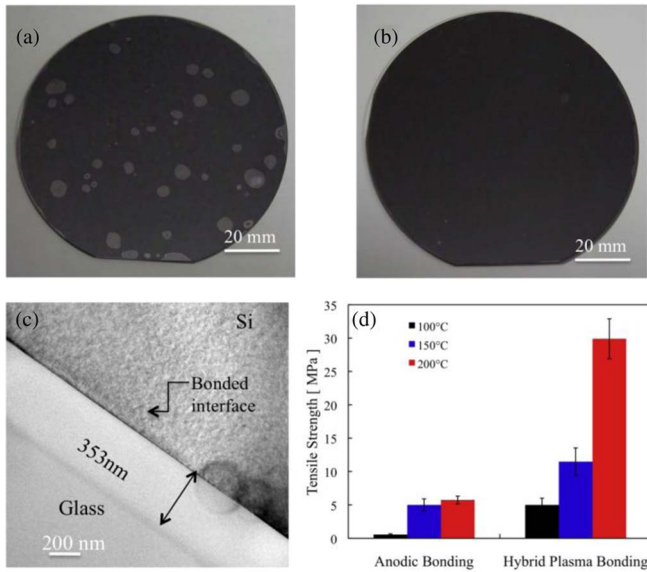


Fig. 16. Optical images of Si/glass wafers bonded in (a) anodic bonding under 1 kV at 200 °C and (b) HPB, and (c) HRTEM image of Si/glass bonded interface and (d) bonding strength as a function of different bonding conditions [65].

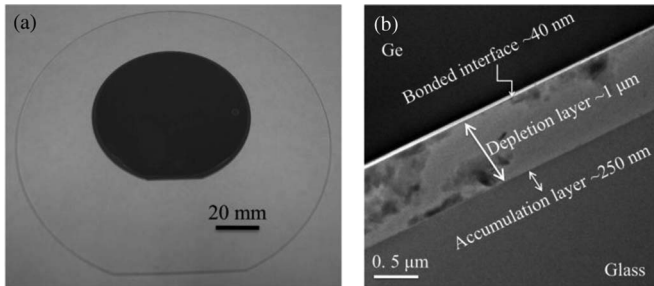


Fig. 17. (a) Optical image, and (b) HRTEM image of HPB Ge/glass interface [67].

improved on increasing the bonding temperature from 100 to 150 °C, it was not considerably changed from 150 to 200 °C. On the other hand, the bonding strength in the HPB at 100 °C was comparable to that in the anodic bonding at 150 and 200 °C. With the increase of the bonding temperature in the HPB, the bonding strength was drastically increased. At 200 °C, the bonding strength in the HPB was 30 MPa, which was significantly higher compared to that from anodic bonding. To the best of our knowledge, this bonding strength was the highest (~30 MPa) compared to the reported values achieved through the conventional anodic bonding. This high-bonding strength in HPB is due to the highly hydrophilic, reactive, and smooth surfaces of Si and glass after sequentially plasma activation. Subsequent anodic treatment resulted in very high electrostatic forces at the bonded interface of Si and glass.

2) *Bonding of Ge/Glass*: HPB has been used for bonding Ge/glass at low temperatures [67]. Fig. 17(a) shows the optical image of the HPB Ge/glass wafers. A nearly void-free interface was achieved using HPB. This is attributed to the absorption of voids in the interfacial oxide. The remaining voids were presumably due to the presence of particles on the activated surface and

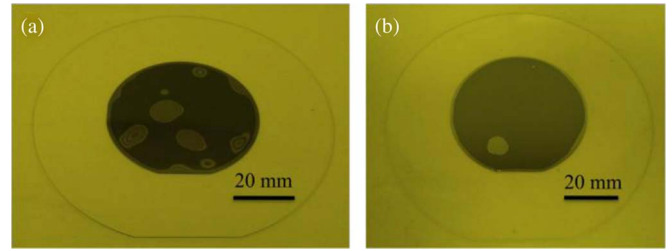


Fig. 18. Optical images of bonded interfaces of GaAs and glass wafers in (a) SPAB at RT and (b) HPB at 200 °C and 1 kV.

entrapment of air at the interface due to plasma-induced surface defects. The bonding strength of Ge/glass interface was 9.1 MPa. This high-bonding strength of the interface is due to the highly hydrophilic and smooth surfaces of Ge and glass after sequential activation [67]. The lower bonding strength of the Ge/glass interface (~9.1 MPa) than the Si/glass interface (~30 MPa) is attributed to the lower bulk fracture strength of Ge than Si or glass.

Fig. 17(b) shows a HRTEM image of bonded Ge/glass interface. A ~1- μm -thick layer (brighter layer than Ge and glass) was observed in glass near the bonded interface. The observed depletion layer in glass was due to the migration of alkaline cations from the region near the interface toward the bulk. In addition to the depletion layer, a ~250-nm-thick second layer in glass was observed near the Ge/glass interface. This is due to accumulation of alkaline cations [67]. Furthermore, a thin layer (~40 nm) with higher contrast than that of the depletion layer was observed at the bonded interface. From energy dispersive X-ray (EDX) analysis, this layer was confirmed as germanium oxide [67].

3) *Bonding of GaAs/Glass*: A relatively new challenge was the integration of GaAs with glass wafer using HPB at 200 °C. Fig. 18 shows the optical images of bonded GaAs and glass using (a) SPAB at room temperature, and (b) HPB at 200 °C. In SPAB, significant numbers of voids were observed at the interface. This is due to the absence of electrostatic force in SPAB. On the other hand, in HPB, a nearly void-free interface was achieved. This is due to the combined effect of electrostatic force and adhesion between the hydrophilic surfaces. The bonding of GaAs/glass can find applications in optical fiber receivers, where the GaAs photodetector bonds with the fiber end.

The HPB mechanism can be summarized as follows. The sequential plasma activation provides highly hydrophilic, reactive, and smooth surfaces. After anodic treatment, the reverse transportation of anions and cations results in an oxide layer across the interface. The oxide layer helps in absorbing the interfacial voids. Therefore, a void-free interface was achieved. The high-bonding strength in HPB is attributed to the combined effect of adhesion between the highly hydrophilic and reactive surfaces, and the electrostatic forces produced during anodic bonding.

V. CONCLUSION

Surface-activation-based nanobonding techniques have been developed to address the current packaging and integration

challenges of electronic, photonic, and fluidic devices. Four nanobonding techniques have been demonstrated for bonding a wide range of materials. Nanobonding in UHV has been utilized for ultrahigh-density interconnection of copper (Cu) nanobumps, and 3-D integration of Au-SBs with Cu-TSVs at room temperature. Further, nanobonding in UHV has been performed at room temperature for diverse range of semiconductors, such as Si/Si, Si/GaAs, Si/InP, and GaP/GaAs. Void-free, strong, and atomic-scale bonding was confirmed. The I - V characteristics of the nanobonded interface were similar to the typical monolithic p-n junction. The perfectly bonded interfaces of similar and dissimilar semiconductors will find significant applications in electronics and optoelectronics, for example.

Successful bonding of ionic material (LiNbO_3) with Si has been demonstrated using an ultrathin Fe nanoadhesion layer at room temperature. The void-free and strong bonding of Si/ LiNbO_3 will find important applications in the fabrication of optical waveguides, optoelectronic modulators, piezoelectric, and MW tunable devices.

In order to extend the applicability of nanobonding for biomedical microsystems, flexible laminations of Cu and LCP have been successfully bonded at low temperature. The bonded interface was smooth and strong, and offered threefold lower loss as compared to the conventional heat lamination.

For nanobonding in air at room temperature, a SPAB technique has been developed. The O_2 RIE plasma followed by MW N_2 radicals was the best combination for sequential plasma activation. The SPAB has been implemented for a wide range of materials including Si/Si, Si/Ge, SiO_2/Ge , and glass/glass. The SPAB was not only reliable at room temperature, but also in high-temperature environments. The nanoscale and strong bonding in SPAB at room temperature and in air will find significant applications in low-cost MEMS/NEMS, microfluidics, photonic, and optoelectronic applications.

Finally, for nanobonding of ionic materials with semiconductors, a novel HPB technique has been developed. The HPB has been demonstrated for Si/glass, Ge/glass, and GaAs/glass at 200°C . Void-free, strong, and nanoscale bonding of diverse materials in HPB will open up opportunities in microfluidics, lab-on-a-chip, and photodetector applications.

ACKNOWLEDGMENT

The author (M. M. R. Howlader) would like to thank Dr. A. Shigetou at the National Institute for Materials Science, Tsukuba, Japan for her contribution to this work. The authors would like to thank Prof. M. J. Kim for the contribution of nanointerfacial characterization. They would also like to thank M. G. Kibria and F. Zhang for their contributions in the experiments and in the write-up and compilation of the paper.

REFERENCES

- [1] N. Tanaka, Y. Yoshimura, M. Kawashita, T. Uematsu, C. Miyazaki, N. Toma, K. Hanada, M. Nakanishi, T. Naito, T. Kikuchi, and T. Akazawa, "Through-silicon via interconnection for 3D integration using room-temperature bonding," *IEEE Trans. Adv. Packag.*, vol. 32, no. 4, pp. 746–753, Nov. 2009.
- [2] N. Miki, X. Zhang, R. Khanna, A. A. Ayón, D. Ward, and S. M. Spearing, "Multi-stack silicon-direct wafer bonding for 3D MEMS manufacturing," *Sens. Actuators A Phys.*, vol. 103, no. 1–2, pp. 194–201, Jan. 2003.
- [3] S. Lai, H. Y. Lin, and C. T. Hu, "Effect of surface treatment on wafer direct bonding process," *Mater. Chem. Phys.*, vol. 83, no. 2–3, pp. 265–272, Feb. 2004.
- [4] B. Swinnen, W. Ruythooren, P. De Moor, L. Bogaerts, L. Carbonell, K. De Munck, B. Eyckens, S. Stoukatch, D. Sabuncuoglu, Z. Tökei, J. Vaes, J. Van Aelst, and E. Beyne, "3D integration by Cu–Cu thermo-compression bonding of extremely thinned bulk-Si die containing 10 pitch through-Si vias," presented at the IEDM Conf., San Francisco, Dec. 2006.
- [5] Z. R. Huang, D. Guidotti, L. Wan, Y.-J. Chang, J. Yu, J. Liu, H.-F. Kuo, G.-K. Chang, F. Liu, and R. R. Tummala, "Hybrid integration of end-to-end optical interconnects on printed circuit boards," *IEEE Trans. Compon. Packag. Technol.*, vol. 30, no. 4, pp. 708–715, Dec. 2007.
- [6] T. D. Wang and J. V. Dam, "Optical biopsy: A new frontier in endoscopic detection and diagnosis," *Clin. Gastroenterol. Hepatol.*, vol. 2, no. 9, pp. 744–753, 2004.
- [7] International technology roadmap for semiconductors (ITRS), 2005, pp. 42.
- [8] Medtronic Sigma Implantable Pacemakers. (2005). [Online]. Available: [http://www.dhsspsni.gov.uk/niaic-mdea\(ni\)2005_95.pdf](http://www.dhsspsni.gov.uk/niaic-mdea(ni)2005_95.pdf)
- [9] A. Shigetou, T. Itoh, M. Matsuo, N. Hayasaka, K. Okumura, and T. Suga, "Bumpless interconnect through ultrafine Cu electrodes by means of surface-activated bonding (SAB) Method," *IEEE Trans. Adv. Packag.*, vol. 29, no. 2, pp. 218–226, May 2006.
- [10] Q. Wang, Z. Xu, M. M. R. Howlader, T. Itoh, and T. Suga, "Reliability and microstructure of Au-Al and Au-Cu direct bonding fabricated by the surface activated bonding," in *Proc. Electron. Comp. Technol. Conf.*, San Diego, CA, 2002, pp. 915–919.
- [11] M. M. R. Howlader, A. Yamauchi, and T. Suga, "Surface activation based nano-bonding and interconnection at room temperature," *J. Micromech. Microeng.*, to be published.
- [12] M. M. R. Howlader, F. Zhang, M.G. Kibria, T. Suga, and A. Yamauchi, "Surface activated bonding of copper through silicon vias and gold stud bumps at low temperature," in *Proc. Int. Conf. Electron. Packag.*, Japan, 2010, pp. 149–154.
- [13] P.-I. Wang, S. H. Lee, T. C. Parker, M. D. Frey, T. Karabacak, J.-Q. Lu, and T.-M. Lu, "Low temperature wafer bonding by copper nanorod array," *Electrochem. Solid-State Lett.*, vol. 12, no. 4, pp. H138–H141, Apr. 2009.
- [14] C.-F. Chou, J. Gu, Q. Wei, Y. Liu, R. Gupta, T. Nishio, and F. Zenhausern, "Nanopatterned structures for biomolecular analysis towards genomic and proteomic applications," in *Proc. SPIE*, 2005, vol. 5592, pp. 183–192.
- [15] H. Takagi, R. Maeda, and T. Suga, "Wafer-scale spontaneous bonding of silicon wafers by argon-beam surface activation at room temperature," *Sens. Actuators A Phys.*, vol. 105, no. 1, pp. 98–102, Jun. 2003.
- [16] M. M. R. Howlader and F. Zhang, "Void-free strong bonding of surface activated silicon wafers from room temperature to annealing at 600°C ," *Thin Solid Films*, vol. 519, pp. 804–808, Nov. 2010.
- [17] M. M. R. Howlader, T. Watanabe, and T. Suga, "Investigation of the bonding strength and interface current of p-Si/n-GaAs wafers bonded by surface activated bonding at room temperature," *J. Vac. Sci. Technol. B*, vol. 19, no. 6, pp. 2114–2118, Nov. 2001.
- [18] T. R. Chung, L. Yang, N. Hosoda, H. Takagi, and T. Suga, "Wafer direct bonding of compound semiconductors and silicon at room temperature by the surface activated bonding method," *Appl. Surf. Sci.*, vol. 117/118, pp. 808–812, Jun. 1997.
- [19] M. M. R. Howlader, T. Watanabe, and T. Suga, "Characterization of the bonding strength and interface current of p-Si/n-InP wafers bonded by surface activated bonding method at room temperature," *J. Appl. Phys.*, vol. 91, no. 5, pp. 3062–3066, Mar. 2002.
- [20] M. M. R. Howlader, T. Suga, and M. J. Kim, "Wafer level and chip size direct wafer bonding at room temperature," in *Proc. 206th Electrochem. Soc. Meet.*, Honolulu, HI, 2004, p. 1423.
- [21] M. M. R. Howlader, T. Suga, F. Zhang, T. H. Lee, and M. J. Kim, "Interfacial behavior of surface activated p-GaP/n-GaAs bonded wafers at room temperature," *Electrochem. Solid-State Lett.*, vol. 13, no. 3, pp. H61–H65, Mar. 2010.
- [22] K. Sakurai, H. Yokoi, T. Mizumoto, D. Miyashita, and Y. Nakano, "Fabrication of semiconductor laser for integration with optical isolator," *Jpn. J. Appl. Phys.*, vol. 43, no. 4 A, pp. 1388–1392, Apr. 2004.
- [23] T. Mizumoto, H. Saito, K. Sakurai, and Y. Shoji, "Wafer bonding of magneto-optic garnet and its application to waveguide optical devices," *ECS Trans.*, vol. 3, no. 39, pp. 11–22, 2007.

- [24] H. Saito, M. M. R. Howlader, T. Mizumoto, and T. Suga, "Surface activated bonding for optical isolator," submitted for publication.
- [25] Y. Shoji, T. Mizumoto, H. Yokoi, I. W. Hsieh, and R. M. Osgood, Jr., "Magneto-optical isolator with silicon waveguides fabricated by direct bonding," *Appl Phys Lett.*, vol. 92, no. 7, pp. 071117-1–071117-3, Feb. 2008.
- [26] M. M. R. Howlader, T. Suga, and M. J. Kim, "A novel bonding method for ionic wafers," *IEEE Trans. Adv. Packag.*, vol. 30, no. 4, pp. 598–604, Nov. 2007.
- [27] M. M. R. Howlader, H. Okada, T. H. Kim, T. Itoh, and T. Suga, "Wafer-level surface-activated bonding tool for MEMS packaging," *J. Electrochem. Soc.*, vol. 151, no. 7, pp. G461–G467, Jul. 2004.
- [28] T. Uelzen, S. Fandrey, and J. Muller, "Wafer-level surface-activated bonding tool for MEMS packaging," *Microsyst. Technol.*, vol. 12, pp. 343–351, 2006.
- [29] K. W. Oh, A. Han, S. Bhansali, and C. H. Ahn, "A low-temperature bonding technique using spin-on fluorocarbon polymers to assemble Microsystems," *J. Micromech. Microeng.*, vol. 12, no. 2, pp. 187–191, Mar. 2002.
- [30] A. H. Forster, M. Krihak, P. D. Swanson, T. C. Young, and D. E. Ackley, "A laminated, flex structure for electronic transport and hybridization of DNA," *Biosens. Bioelectr.*, vol. 16, no. 3, pp. 187–194, May 2001.
- [31] T. Stieglitz, H. Beutel, and J.-U. Meyer, "Microflex—A new assembling technique for interconnects," *J. Intell. Mater. Syst. Struct.*, vol. 11, no. 6, pp. 417–425, 2000.
- [32] M. M. R. Howlader, M. Iwashita, K. Nanbu, K. Saijo, and T. Suga, "Enhanced Cu/LCP adhesion by pre-sputter cleaning prior to Cu deposition," *IEEE Trans. Adv. Packag.*, vol. 28, no. 3, pp. 495–502, Aug. 2005.
- [33] K. Nanbu, S. Ozawa, K. Yoshida, K. Saijo, and T. Suga, "Low temperature bonded Cu/LCP materials for FPCs and their characteristics," *IEEE Trans. Compon. Packag. Technol.*, vol. 28, no. 4, pp. 760–764, Dec. 2005.
- [34] M. M. R. Howlader, T. Suga, A. Takahashi, K. Saijo, S. Ozawa, and K. Nanbu, "Surface activated bonding of LCP/Cu for electronic packaging," *J. Mater. Sci.*, vol. 40, no. 12, pp. 3177–3184, Jun. 2005.
- [35] P. Laurens, S. Petit, and F. A.-Khonsari, "Study of PET surfaces after laser or plasma treatment: Surface modifications and adhesion properties towards Al deposition," *Plasmas. Polym.*, vol. 8, no. 4, pp. 281–295, Dec. 2003.
- [36] J. S. Cho, W. K. Choi, S. K. Koh, and K. H. Yoon, "Metallization of Cu on polytetrafluoroethylene modified by keV Ar⁺ ion irradiation," *J. Vac. Sci. Technol.-B*, vol. 16, no. 3, pp. 1110–1114, May 1998.
- [37] J. M. Burkstrand, "Electron spectroscopic study of oxygen-plasma-treated polymer surfaces," *J. Vac. Sci. Technol B*, vol. 15, no. 2, pp. 223–226, Mar. 1978.
- [38] N. J. Chou and C. H. Tang, "Interfacial reaction during metallization of cured polyimide: An XPS study," *J. Vac. Sci. Technol A*, vol. 2, no. 2, pp. 751–755, Apr. 1984.
- [39] S. K. Koh, S. C. Park, S. R. Kim, W. K. Choi, H. J. Jung, and K. D. Pae, "Surface modification of polytetrafluoroethylene by Ar⁺ irradiation for improved adhesion to other materials," *J. Appl. Polym. Sci.*, vol. 64, no. 10, pp. 1913–1921, Jun. 1997.
- [40] G. S. Chang, K. H. Chae, C. N. Whang, E. Z. Kurmaev, D. A. Zatsepin, R. P. Winarski, D. L. Ederer, A. Moewes, and Y. P. Lee, "Mechanism for interfacial adhesion strength of an ion beam mixed Cu/polyimide with a thin buffer layer," *Appl. Phys. Lett.*, vol. 74, no. 4, pp. 522–524, Jan. 1999.
- [41] C. Li, F. E. Sauser, R. G. Azizkhan, C. H. Ahn, and I. Papautsky, "Polymer flip-chip bonding of pressure sensors on a flexible Kapton film for neonatal catheters," *J. Micromech. Microeng.*, vol. 15, no. 9, pp. 1729–1735, Sep. 2005.
- [42] C. L. F. Ma, M. J. Deen, and L. Tarof, "Characterization and Modeling of SAGCM InP/InGaAs avalanche photodiodes for multigigabit optical fiber communications," in *Advances in Imaging and Electron Physics*, vol. 99, P. Hawkes, Ed., San Diego, CA: Academic, 1998, pp. 65–170.
- [43] C. L. F. Ma, M. J. Deen, L. Tarof, and J. Yu, "Temperature dependence of breakdown voltages in separate absorption, grading, charge and multiplication InP/InGaAs avalanche photodiodes," *IEEE Trans. Electron Devices*, vol. 42, no. 5, pp. 810–818, May 1995.
- [44] M. Margarit, J. L. Tham, R. G. Meyer, and M. J. Deen, "A low-noise, low-power VCO with automatic amplitude control for wireless applications," *IEEE J. Sol.-Stat. Circuits*, vol. 34, no. 6, pp. 761–771, Jun. 1999.
- [45] M. Jamal Deen, R. Murji, A. Fakhr, N. Jafferli, and W. L. Ngan, "Low power CMOS integrated circuits for radio frequency applications," *IEE Proc. - Circ. Dev. Syst.*, vol. 152, no. 5, pp. 509–522, Oct. 2005.
- [46] M. W. Shinwari, M. J. Deen, and D. Landheer, "Study of the electrolyte-insulator-semiconductor field-effect transistor (EISFET) with applications in biosensor design," *Microelectron. Reliab.*, vol. 47, no. 12, pp. 2025–2057, Dec. 2007.
- [47] B. Jaggi, M. J. Deen, and B. Palcic, "Quantitative light microscope using a solid state detector in the primary image plane," U.S. Patent 4845552, Jul. 4, 1989.
- [48] M. Kfourri, O. Marinov, P. Quevedo, N. Faramarzpour, S. Shirani, L. W.-C. Liu, Q. Fang, and M. J. Deen, "Towards a miniaturized wireless fluorescence-based diagnostic imaging system," *IEEE J. Select. Top. Quantum Electron.*, vol. 14, no. 1, pp. 226–234, Jan./Feb. 2008.
- [49] C. W. Chu, M. J. Deen, and R. H. Hill, "Sensors for detecting sub-ppm NO₂ Using photochemically produced amorphous tungsten Oxide," *J. Electrochem. Soc.*, vol. 145, no. 12, pp. 4219–4225, Dec. 1998.
- [50] T. Suga, T. H. Kim, and M. M. R. Howlader, "Combined process for wafer direct bonding by means of the surface activation method," in *Proc. ECTC Conf.*, vol. 1, 2004, pp. 484–490.
- [51] F. Zhang, M. G. Kibria, K. Cormier, and M. M. R. Howlader, "Surface and interface characterization of sequentially plasma activated silicon, silicon dioxide and germanium wafers for low temperature bonding applications," *ECS Trans.*, vol. 33, no. 4, pp. 329–338, 2010.
- [52] M. M. R. Howlader, T. Suga, H. Itoh, T. H. Lee, and M. J. Kim, "Role of heating on plasma activated silicon wafers bonding," *J. Electrochem. Soc.*, vol. 156, no. 11, pp. H846–H851, Nov. 2009.
- [53] M. M. R. Howlader, F. Zhang, and M. G. Kibria, "Void nucleation at a sequentially plasma-activated silicon/silicon bonded interface," *J. Micromech. Microeng.*, vol. 20, no. 6, pp. 065012-1–065012-10, Jun. 2010.
- [54] M. G. Kibria, F. Zhang, T. H. Lee, M. J. Kim, and M. M. R. Howlader, "Comprehensive investigation of sequential plasma activated Si/Si bonded interfaces for nano-integration on the wafer scale," *Nanotechnology*, vol. 21, no. 13, pp. 134011-1–134011-10, Apr. 2010.
- [55] O. I. Dosunmu, D. D. Cannon, M. K. Emsley, B. Ghyselen, L. Jifeng, L. C. Kimerling, and M. S. Unlu, "Resonant cavity enhanced Ge photodetectors for 1550 nm operation on reflecting Si substrates," *IEEE J. Sel. Topics Quantum Electron.*, vol. 10, no. 4, pp. 694–701, Jul./Aug. 2004.
- [56] C. L. F. Ma, M. J. Deen, and L. Tarof, "Multiplication in separate absorption, grading, charge and multiplication InP/InGaAs avalanche photodiodes," *IEEE J. Quantum Electron.*, vol. 31, no. 11, pp. 2078–2089, Nov. 1995.
- [57] Z. X. Yan, M. J. Deen, and D. S. Malhi, "Gate-controlled lateral LPNP BJT: Characteristics, modeling, and circuit applications," *IEEE Trans. Electron Devices*, vol. 44, no. 1, pp. 118–128, Jan. 1997.
- [58] Z. X. Yan and M. J. Deen, "A new resonant-tunnel diode-based multi-valued memory circuit using a MESFET depletion load," *IEEE J. Sol.-Stat. Circuits*, vol. 27, no. 8, pp. 1198–1203, Aug. 1992.
- [59] A. L.-Nordstrom and F. Yndurain, "Geometrical configuration of interstitial oxygen in silicon and in germanium," *Solid State Commun.*, vol. 89, no. 9, pp. 819–822, Mar. 1994.
- [60] M. M. R. Howlader, S. Suehara, and T. Suga, "Room temperature wafer level glass/glass bonding," *Sens. Actuators A Phys.*, vol. 127, no. 1, pp. 31–36, Feb. 2006.
- [61] M. M. R. Howlader, S. Suehara, H. Takagi, T. H. Kim, R. Maeda, and T. Suga, "Room-temperature microfluidics packaging using sequential plasma activation process," *IEEE Trans. Adv. Packag.*, vol. 29, no. 3, pp. 448–456, Aug. 2006.
- [62] Z. Liang, N. Chiem, G. Ocvirk, T. Tang, K. Fluri, and D. J. Harrison, "Microfabrication of a planar absorbance and fluorescence cell for integrated capillary electrophoresis devices," *Anal. Chem.*, vol. 68, no. 6, pp. 1040–1046, Mar. 1996.
- [63] L. Ceriotti, K. Weible, N. F. de Rooij, and E. Verpoorte, "Rectangular channels for lab-on-a-Chip applications," *Microelectron. Eng.*, vol. 67–68, no. 1, pp. 865–871, Jun. 2003.
- [64] A. Shigetou and T. Suga, "Modified diffusion bonding of chemical mechanical polishing Cu at 150 °C at ambient pressure," *Appl. Phys. Expr.*, vol. 2, no. 5, pp. 056501-1–056501-3, 2009.
- [65] M. M. R. Howlader, M. G. Kibria, F. Zhang, and M. J. Kim, "Hybrid plasma bonding for void-free strong bonded interface of silicon/glass at 200 °C," *Talanta*, vol. 82, no. 2, pp. 508–515, Jul. 2010.
- [66] G. Y. Li and L. Wang, "Influence of bonding parameters on electrostatic force in anodic wafer bonding," *Thin Solid Films*, vol. 462–463, pp. 334–338, Sep. 2004.
- [67] M. M. R. Howlader, M. G. Kibria, and F. Zhang, "Hybrid plasma bonding of germanium and glass wafers at low temperature," *Mater. Lett.*, vol. 64, no. 13, pp. 1532–1535, Jul. 2010.



M. M. R. Howlader received the B.Sc.Eng. degree in electrical and electronic engineering from Khulna University of Engineering and Technology, Khulna, Bangladesh, in 1988, and the M.S. and Ph.D. degrees in nuclear engineering from Kyushu University, Fukuoka, Japan, in 1996 and 1999, respectively.

From 2000 to 2005, he was with the Research Center for Advanced Science and Technology, The University of Tokyo, Tokyo, Japan, as an endowed Associate Professor. He is currently an Assistant Professor in the Department of Electrical and Computer

Engineering, McMaster University, Hamilton, ON, Canada. He has authored or coauthored more than 40 refereed papers and more than 65 international proceedings articles. His research interests include the chip-size and wafer-level planar and vertical integration for microelectronics, microelectromechanical systems, optoelectronics packaging, oxidation behavior of solders and electronic materials, interfacial adhesions, radiation effects on materials and packages, nanobonding and packaging of materials, devices, and components for microsystems and nanosystems for health and environmental applications.

Dr. Howlader is a member of the Japan Institute of Electronic Packaging. He was the recipient of the Best Technical Paper Award at the International Conference on Electronic Packaging in 2003.



P. R. Selvaganapathy received the B.S. degree in chemical and electrochemical engineering from Central ElectroChemical Research Institute, Karaikudi, India, in 1998, and the M.S. and Ph.D. degrees in electrical engineering and computer science from the University of Michigan, Ann Arbor, in 2001 and 2002, respectively.

He was engaged in various projects related to microelectromechanical systems (MEMS) and BioMEMS processes and device development including electrochemical detection in capillary electro-

trophoresis systems, electroosmotic pumping systems, thermal phase-change polymers, porous polymers in microsystems, and investigation of microplasmas as a fluorescence excitation source for DNA. From 2003 to 2004, he was a Postdoctoral Research Associate at Bionano Systems, Division of Sandia National Laboratories, Livermore, CA, where he is engaged for the development of an integrated sensing system for low-concentration protein detection with biodefense applications. He is currently an Associate Professor in Mechanical and Biomedical Engineering, McMaster University, Hamilton, ON, Canada. He has authored or coauthored more than 40 publications in journals and conferences and three invited book chapter. He holds three U.S. patents related to MEMS/microfluidic devices. His research interests include the design, fabrication, and development of microdevices for application in biology and medicine, medical and environmental diagnostics, drug delivery, drug discovery, and electronic cooling. He has featured his research work in scientific media, such as *Popular Mechanics* as well as in mainstream media, such as CBC news, and in newspapers across Canada. He was also the recipient of the Early Researchers Award from the Ontario Ministry of Research and Innovation in 2010.



M. Jamal Deen (F'02) was born in Georgetown, Guyana, South America. He received the Ph.D. degree in electrical engineering and applied physics from Case Western Reserve University, Cleveland, OH, in 1985. His Ph.D. dissertation was focused on the design and modeling of a new CARS spectrometer for dynamic temperature measurements and combustion optimization in rocket and jet engines, and was sponsored by NASA, Cleveland.

He is currently a Professor of electrical and computer engineering at McMaster University, Hamilton, ON, Canada, where he is a Senior Canada Research Chair in information technology. He has authored or coauthored more than 420 peer-reviewed articles (about 20% are invited), 14 invited book chapters, and six awarded patents. His research interests include microelectronics/nanoelectronics, optoelectronics, and nanotechnology and their emerging applications.

Dr. Deen was a Fulbright Scholar (under the Latin American scholarship program) from 1980 to 1982, an American Vacuum Society Scholar from 1983 to 1984, and a Natural Science and Engineering Research Council of Canada Senior Industrial Fellow in 1993. He was the recipient of the 2002 Thomas D. Callinan Award from the Electrochemical Society, the Distinguished Researcher Award, Province of Ontario in July 2001, a Humboldt Research Award in 2006, an IBM Faculty Award in 2006, the Eadie Medal from the Royal Society of Canada in 2008, and also seven best paper awards. He is a Distinguished Lecturer of the IEEE Electron Device Society. He was a Fellow in eight national academies and professional societies including the Royal Society of Canada—The Academies of Arts, Humanities, and Sciences of Canada, the Indian National Academy of Engineering (FINAE-Foreign), the American Physical Society, and the Electrochemical Society. He was also an Honorary Member of the World Innovation Foundation—the foundation's highest honor.



T. Suga (M'92) received the M.S. degree in precision engineering from the University of Tokyo, Tokyo, Japan, in 1979, and the Ph.D. degree from the Max-Planck Institut für Metallforschung, University of Stuttgart, Stuttgart, Germany, in 1983. His Ph.D. thesis was focused on fracture mechanics characterization of metal-ceramic interfaces.

In 1984, he was a member of the Faculty of Engineering, the University of Tokyo, where he has been a Professor of precision engineering since 1993. He is a Director with a Research Group, National Institute of Materials Science, Tsukuba, and also a member of the Science Council of Japan. He has authored or coauthored 200 papers and five books in the field of material science and electronic packaging. His current research interests include microsystems integration and packaging, and development of interconnect technology, especially the room temperature bonding technique for various applications.

Prof. Suga was appointed as the 20th council members of the Japan Council of Science on October 2005. He has endeavored to establish collaboration between industries and academia for the packaging technology. He was the Organizer of the foundation of the Institute of Microsystem Integration in 1997, the first consortium for the competitive packaging industry, which is consisting of 30 Japanese companies. He has advocated also the importance of environmental aspects of packaging technology and is well known as the key organizer of Japanese roadmap of lead-free soldering and International Ecodesign Conference.